SOLAR PROMINENCE INTERACTIONS

C. Richard DeVore[1] and Spiro K. Antiochos[2]

Naval Research Laboratory, Washington, DC 20375

and

Guillaume Aulanier

Laboratoire d'Etudes Spatiales et d'Instrumentation en Astrophysique, Observatoire de Paris, 91295 Meudon Cedex, France

ABSTRACT

We report numerical simulations of the formation, interaction, and magnetic reconnection between pairs of solar prominences within the sheared-arcade model. Our experiments consider the four possible basic combinations of chiralities (identical or opposite) and axial magnetic fields (aligned or opposed) between the participating prominences. When the topology of the global flux system comprising the prominences and arcades is bipolar, so that a single polarity inversion line is shared by the two structures, then identical chiralities necessarily imply aligned axial fields, while opposite chiralities imply opposed axial fields. In the former case, external magnetic reconnections forming field lines linking the two prominences occur; in the latter, such reconnections are disfavored, and no linkage takes place. These results concur with empirical rules for prominence interactions. When the topology instead is quadrupolar, so that a second polarity inversion line crossing the first lies between the prominences, then the converse relation holds between chirality and axial-field alignment. External reconnections forming linking field lines now occur between prominences with opposite chiralities; they also occur, but result only in footpoint exchanges, between prominences with identical chiralities. These findings conflict with the accepted empirical rules but may not have been tested in observations to date. All of our model prominences, especially those that undergo linking reconnections, contain substantial magnetic shear and twist. Nevertheless, none exhibits any sign of onset of instability or loss of equilibrium that might culminate in an eruption.

Subject headings: MHD — Sun: magnetic fields — Sun: prominences

1. INTRODUCTION

Solar prominences are complex, intricate, dynamic structures that pose multifaceted challenges to observation and theory. Their fine threads of cold, dense plasma, suspended above the surface in the hot, tenuous corona, are seen in emission as bright clouds at the limb and in absorption as dark filaments against the disk. The magnetic fields that guide these threads, thermally insulate them from their surroundings, and support them against gravity are directly measurable only in the optically thick cores and chromospheric feet of prominences. This circumstance, together with the highly complex interplay of plasma and magnetic field dynamics that forms, maintains, and eventually destroys these structures, opens a path for numerous contending explanations of the prominence phenomenon (see, e.g., Tandberg-Hanssen 1974, 1995; Priest 1989; Ruzdjak & Tandberg-Hanssen 1990; Webb et al. 1998).

Early observations in the lowest Balmer line of hydrogen, Hα, revealed some of the dynamic range of filament behavior (d'Azambuja & d'Azambuja 1948). Both quite short- and very long-lived prominences, with lifetimes ranging from a day or two to several weeks, were recorded. Some appeared to dissolve away slowly, but in many instances the disappearance was very sudden ("disparition brusques"), an occurrence that we now understand signals a prominence eruption. Less dramatic, day-to-day evolutionary changes that were observed include the merger of neighboring but distinct filaments to form an evidently newly linked, continuous structure, as well as the inverse process of fragmentation. The d'Azambujas referred to these linking and fragmenting segments as complex filaments ("des filaments complexes").

The advent of the magnetograph (Babcock 1953) greatly enlarged the scope of inquiries into the nature of prominences. It was promptly shown (Babcock & Babcock 1955) that filaments form at the boundaries between large-scale regions of opposed polarities of the Sun's radial magnetic field, i.e., at polarity inversion lines, and are approximately aligned with them. During the next decade, direct measurements of the magnetic fields within prominences became possible, first in the strong (100 G) fields of active region filaments (Zirin & Severny 1961), and later in the weak (10 G or less) fields of quiescent filaments (Rust 1967). Rust's field measurements of the high-latitude, polar crown filaments led him to discover their preferred magnetic orientation: at that epoch in sunspot cycle 20, the fields of the northern crown of filaments essentially all pointed east to west, while those of filaments in the southern crown pointed west to east. These filaments tend to be long-lived and to link and fragment among themselves, as described previously by the d'Azambujas. Thus, in the case of the polar crown at least, linking filaments were found to have aligned axial magnetic fields.

Subsequent studies have confirmed these early results on prominence location, orientation, and interactions and have revealed many additional details on the environment in which they form (see Martin [1998] for a comprehensive review, or Martin [2001] for a concise summary). The region encompassing the polarity inversion line (PIL) above which a prominence forms has been found to host chromospheric fibrils that strongly align themselves with the PIL (Foukal 1971), rather

---

than bridging over it, as is more typical. These fibrils also reverse direction as the PIL is crossed, suggesting that the low-lying magnetic field there is very strongly sheared, i.e., also approximately aligned with the polarity inversion. This configuration is referred to as a filament channel (Gaizauskas 2001). The alignment of the fibrils relaxes with increasing distance from the PIL, as does that of the field, and the configuration transitions to a much more nearly potential (current-free) arcade overlying the PIL, enclosing both the filament channel at the surface and the filament itself in the corona. The filament channel is more fundamental, extensive, and persistent than the filament(s) it contains: the latter can form, fragment and/or link, erupt, even reform, all the while leaving the progenitor channel otherwise undisturbed.

Measurements show that the axial fields of a channel, its filaments, and its overlying arcade are always aligned. When observed from the positive-polarity side of the PIL, these fields can point either to the right or to the left. These configurations have been designated to possess "dextral" and "sinistral" chiralities, respectively (Martin et al. 1994; Zirker 2001). Due to the invariant alignment of channel and filament fields, multiple filaments formed within any single channel always will have their axial fields aligned. As with the polar-crown filaments measured by Rust, pairs of filaments with identical chirality—whether dextral or sinistral—are able to link up with one another if brought into contact. Martin et al. provide a beautiful example of an oval filament formed in this way, in Hα images from 1990 March 4. Van Ballegooijen (2004) displays an evolutionary sequence of images from 1998 June 16–21, showing the linking of two filaments into a conjoined U shape, whose magnetostatic equilibrium he then models. On other occasions, however, filament channels of opposite chiralities, and their filaments with opposed axial fields, come into proximity and interact. In these cases, the neighboring ends have been observed to avoid each other and form a cusp. Martin et al. illustrate this with a mixed filament pair (one dextral, one sinistral) on 1991 September 1; Rust (2001) also cites this example to demonstrate the phenomenon. Schmieder et al. (2004) found both types of evolution occurring in a complex active region during 1998 September 8–11, wherein three dextral segments joined to form one leg of a V, with a sinistral filament on the other leg and a cusp separating them. Note that in all cases, these findings of linkage or avoidance refer to observations of the prominence plasma, rather than of the coronal magnetic field, which is far more difficult to measure directly and so can only be inferred.

Previously, we have investigated the properties of individual prominences modeled as differentially sheared arcades. Such structures fit naturally with the observed properties of filament channels, whose strong magnetic shear is concentrated near the polarity inversion line of the vertical field, with the field direction rotating toward an essentially potential arcade on the surface well away from the PIL and in the corona overlying the filament itself. The shear aligns the magnetic field and its entrained plasma threads with the PIL, as observed. Meanwhile, the overlying arcade prevents the sheared core flux from rising freely, forming first flattened and then dipped field lines whose tension can support the prominence plasma against gravity (Antiochos et al. 1994). As the shear increases, the competition between magnetic tension and pressure also rotates the flattened and dipped field lines in the horizontal plane. This causes the component of the prominence field transverse to the underlying PIL to transition from purely normal polarity to mixed, but predominantly inverse, polarity (Aulanier et al. 2002). At sufficiently large shear, multiple reconnections between the prom-

inence core field and the inner parts of the restraining arcade produce helically wound field lines that envelope the prominence body (DeVore & Antiochos 2000), much like those frequently observed in preeruptive and eruptive filaments.

We now have conducted numerical simulations of interacting pairs of solar prominences based on the sheared-arcade model. In this paper, we describe the dynamics, reconnection, and stability of the prominence magnetic fields during these interactions. We infer that the observed linkages or avoidances of the filament plasmas during these encounters reflect the formation, or absence of formation, of similar linkages between their magnetic fields. In a subsequent paper (Aulanier et al. 2005), we shall describe and interpret the inferred plasma structures associated with our magnetic configurations. We begin here by considering the two scenarios suggested by the observations cited earlier: identical chiralities with aligned axial magnetic fields, and opposite chiralities with opposed axial fields. Both occur in simple bipolar distributions of vertical magnetic flux, in which a single polarity inversion line is shared by the converging structures. We then complete the basic set of combinations of chiralities and axial fields by turning to two additional scenarios: identical chiralities with opposed axial fields, and opposite chiralities with aligned axial fields. In these cases, the vertical flux distribution assumes a quadrupolar, 2×2 checkerboard pattern, in which the PIL shared by the two filaments is crossed by a second PIL lying between them. It is likely that these more complex quadrupolar configurations occur far less often than the simpler bipolar ones, and we are unaware of any observational reports describing the resultant prominence evolution. Our simulations provide clear predictions of the behaviors to be expected during these apparently rare encounters.

2. MODEL

The physical prominence model that we employ necessarily comprises a time-dependent, fully three-dimensional magnetoplasma, but it is intuitively relatively simple. We begin with the potential magnetic field due to a pair of identical horizontal point dipoles, set at equal depths below the base plane of our model and with their axes aligned. This magnetic configuration is shown in the left panels of Figure 1. We then evolve the system by imposing differential footpoint motions over a subset of the base plane, concentrated near the polarity inversion line of the vertical magnetic field and directed parallel to it, with the direction of motion reversing across the PIL. This pattern of imposed motions, which accelerate gently from rest, reach their peak, and then decelerate gradually back to rest, is also illustrated in the figure. Whereas on the Sun, the magnetic shear and filament formation evidently arise from a combination of shear or twist in the emergent active region fields (Pevtsov et al. 2003) and subsequent localized surface motions (Chae et al. 2001; Glover et al. 2001; Moon et al. 2002), for simplicity we employ the latter only. Near the conclusion of the episode of footpoint motions, the field attains the configuration shown in the right panels of Figure 1, wherein two model prominence structures have formed. Subsequently, the field relaxes dynamically with all footpoints held fixed. The ends of our two prominences are in close proximity to one another, and as we show below, they interact strongly.

The evolution of the magnetic field and plasma is simulated using our magnetohydrodynamics code FCTMHD3D (see DeVore & Antiochos 2000 for details), which solves the ideal MHD equations in three Cartesian dimensions and time. We are concerned here with the magnetic structure and development, but not the plasma thermodynamics, of prominences in the low corona. Thus, for simplicity we neglect gravity, atmospheric
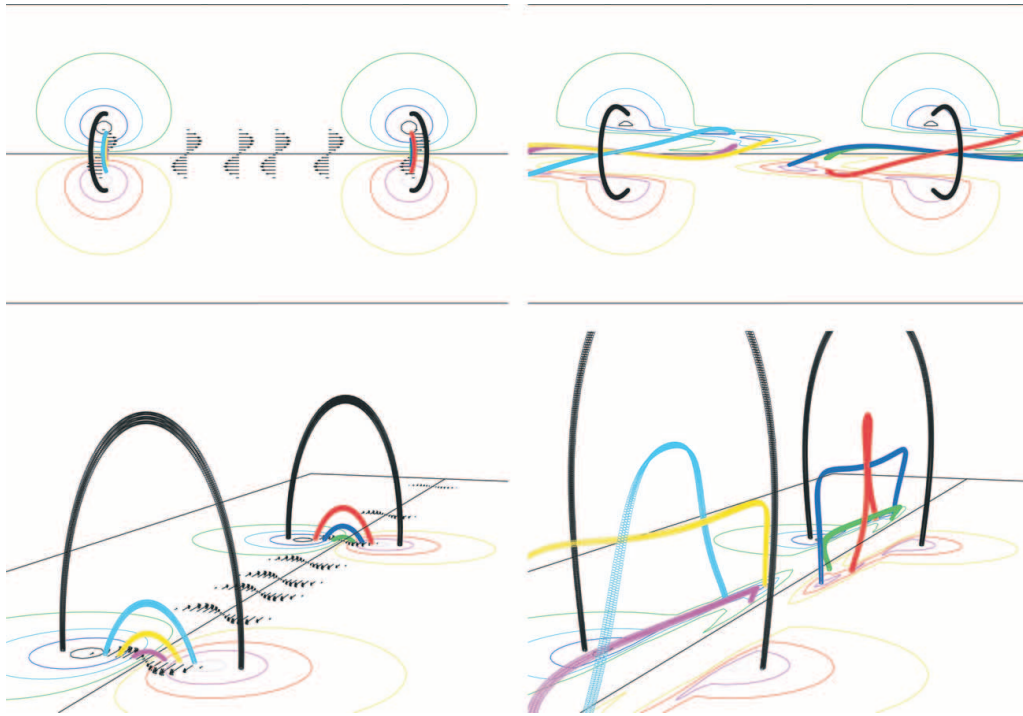
Fɪɢ. 1.—Experiment 1. Overhead (*top*) and perspective (*bottom*) views of interacting dextral prominences, for both the initial state ($t = 0$; *left*) and the configuration near the end of the formation phase and the beginning of the interaction phase ($t = 40$; *right*). Thin lines on the bottom surface are contours of constant vertical magnetic field (*red*, positive; *blue*, negative), with the polarity inversion drawn in black. Thick loops are selected magnetic field lines. Black arrows in the left panels show the direction and relative magnitudes of the footpoint displacements imposed to form the prominence fields and bring them into contact. The axial fields of both prominences point from left to right (*top*) or foreground to background (*bottom*). A vertical expansion factor of 2 is used in this and all other field configurations shown in the paper, to accentuate the vertical structure of the field. This simulation is described in § 3.1.

heating, thermal conduction, and radiation, and treat the corona as an initially uniform, low-pressure, adiabatic plasma. The magnetic field then will be approximately force-free everywhere and at all times, so long as the imposed motions are sufficiently slow. Although the induction equation solved does not include the resistive term explicitly, the numerical dissipation implicit in all convection algorithms permits reconnection to occur where the field gradient is sufficiently strong, i.e., at current sheets.

For computational convenience, we make the MHD equations dimensionless by extracting characteristic values for the mass density ρ_c, magnetic field strength B_c, and spatial scale L_c. Other quantities then are normalized by appropriate combinations of these three parameters. We use this freedom to set the initially uniform mass density $\rho_0 = 1$, dipole field strength $B_0 = 4$, and dipole depth $d = 2$, whence the characteristic Alfvén speed $c_A = B_0/(4\pi\rho)^{1/2} = 1.13$. The initially uniform plasma pressure is $P_0 = 0.010$, corresponding to a minimum plasma beta $8\pi P/B^2 = 0.016$.

Our Cartesian coordinate system has x oriented along the shared polarity inversion line, y perpendicular to this PIL in the base plane, and z in the vertical direction. The scalar potential for the dipole positioned at $(s, 0, -d)$ and directed along y is

$$\phi(x, y, z) = B_0 d^3 y \left[(x - s)^2 + y^2 + (z + d)^2 \right]^{-3/2},$$

whose corresponding magnetic field in the half-space $z \geq 0$ reaches its maximum magnitude ($\approx B_0$) at $x = s$, $y = \pm d/2 = \pm 1$, and $z = 0$. The footpoint displacements at the base plane $z = 0$ are $\delta y = 0$ and

$$\delta x(x, y, t) = \delta s f(t) g(y),$$

where the temporal profile is

$$f(t) = t/\tau - (1/2\pi) \sin(2\pi t/\tau)$$

and the y spatial profile is

$$g(y) = \begin{cases} \sin(\pi y/w) & |y| \leq w, \\ 0 & \text{otherwise.} \end{cases}$$

Parameterizing these motions are the peak displacement $\delta s = 6$, duration $\tau = 50$, and width $w = 1$.

In addition to the specified tangential velocity $\mathbf{v}_t$ implied by the above displacement δx, the boundary conditions at the base plane are that the normal velocity be reflection-symmetric, $v_n = 0$, and the mass and energy densities and the magnetic field components have zero gradient normal to the boundary. Zero-gradient conditions are imposed on all variables at the open top and four side planes of the simulation, thereby allowing the plasma and magnetic field to escape freely through those surfaces should the evolution drive such an outflow. Our simulation domain covers the interval $[-24, +24] \times [-6, +6] \times [0, 12]$, placing the outer boundaries well away from the strong core fields of our structures. The grid is stretched exponentially in all directions from the origin, where the spacing is 0.024, ultimately by factors of 10 along x and 5.5 along y and z. This results in a grid of $500 \times 190 \times 190$ cells.

3. RESULTS

We performed numerical experiments to test each of the four possible combinations of chiralities and axial fields in a pair of interacting prominence: identical or opposite chiralities, and aligned or opposed axial fields. The geometries are illustrated
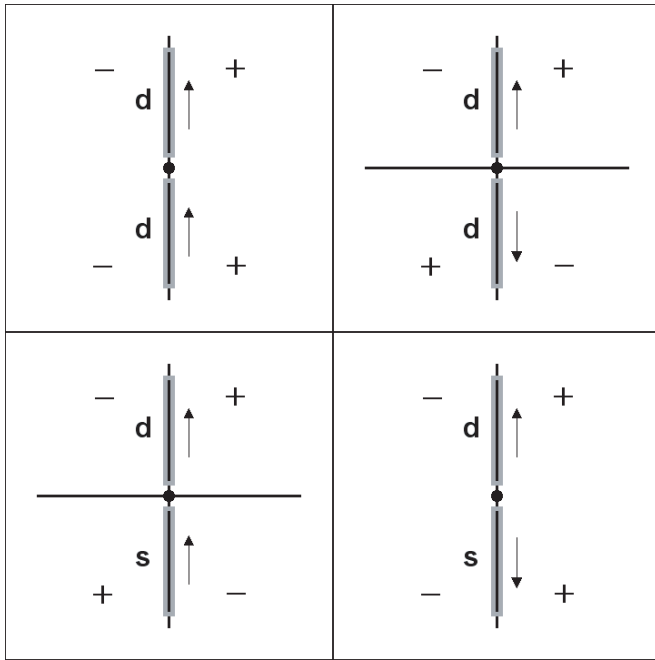
Fig. 2.—Schematic diagram of the four possible configurations of interacting prominences: identical (*top*) or opposite (*bottom*) chiralities, and aligned (*left*) or opposed (*right*) axial magnetic fields. Black lines are the polarity inversion lines of the vertical field, whose direction is denoted by "+" (upward) and "−" (downward); shaded gray rectangles are the prominences, whose chiralities are indicated by "d" (dextral) and "s" (sinistral) and whose axial field directions are shown by the arrows; and filled black circles mark the prominence interaction regions.

schematically in Figure 2. Cases with identical chiralities are shown in the top panels, and those with opposite chiralities in the bottom panels; cases with aligned axial fields are depicted at the left, and those with opposed axial fields at the right. The cited observational examples all fall into either the top left category (identical chiralities with aligned axial fields) or the bottom right category (opposite chiralities with opposed axial fields). They occur in simple, bipolar distributions of vertical magnetic field where a single polarity inversion line is shared by the two filaments. The other configurations require more complex, quadrupolar distributions of vertical field, with a second PIL crossing the one shared by the filaments. In this topology, identical chiralities imply opposed axial fields (*top right*), while opposite chiralities imply aligned axial fields (*bottom left*). We describe our results for each case in turn.

3.1. *Identical Chiralities with Aligned Axial Fields*

This experiment simulates the scenario at the top left in our schematic of prominence interactions, Figure 2. As shown in Figure 1, the dipoles were placed initially at $x = s = \pm 6$, and the two prominences are nearly fully formed at time $t = 40$ (the duration of the imposed motions is $\tau = 50$). If far removed from one another, they would be identical to each other and also to the single, small-shear prominence that we simulated and analyzed in our previous studies. The prominence fields possess dextral chirality, since the axial components point to the right if viewed from the positive-polarity side of the PIL. Dipped portions of the core field lines (e.g., those drawn in blue and yellow) cross the PIL in the opposite direction from the overlying arcade fields. Thus, our prominences are predominantly inverse polarity. The slightly dipped to flat field lines low down (*green and magenta*) show the same behavior. However, weakly arched to flat field

lines high up in the prominences (*red and cyan*) exhibit normal polarity, as we have found previously (Aulanier et al. 2002). These lines also show that the inner arcade fields overlying the prominences are left-skewed, i.e., follow the turns of a left-handed screw, as observed for dextral filaments (Martin & McAllister 1996). Consequently, the whole configuration contains a net negative magnetic helicity (see, e.g., Berger 1998), as we have established previously (DeVore & Antiochos 2000).

This first example, therefore, models the formation of and interaction between two dextral filaments in a dextral filament channel, such as the northern polar crown filaments observed by Rust (1967) or the merging fragments studied by Schmieder et al. (2004). Its complementary configuration of sinistral channel and filaments, right-skewed arcades, and positive helicity can be realized merely by reversing the direction of our imposed footpoint motions, or more simply by creating the mirror image of Figure 1. That case would model Rust's southern polar crown filaments, as well as the interactions that formed oval (Martin et al. 1994) and U-shaped (van Ballegooijen 2004) sinistral filaments from more-or-less rectilinear progenitors.

Previously, we found that internal current sheets can form and promote reconnections between the strongly sheared core fields and the unsheared inner arcade fields of each individual structure, when the footpoint displacement becomes sufficiently large (DeVore & Antiochos 2000). This results from the leaning of the strongly sheared field across the polarity inversion line, into the regions of weak field on the far side of the PIL, which brings the trailing portions of these field lines into contact with the arcade fields on the far side of the PIL. Our present series of experiments exhibits an intricate sequence of such events. In this case, the close approach of the strong core fields in the interaction region distorts the prominence fields, creating the internal current sheets and instigating the reconnections within each structure at more modest footpoint displacements than before. These internal rearrangements occur irrespective of whether any external reconnections take place to form linking field lines joining the two filaments. We describe details of this process for our first experiment only, although the consequences are evident in images from our later experiments as well.

Figure 3 shows part of the reconnection sequence for the dextral filament in the background. A similar sequence reconfigures the fields of the foreground filament, but it is omitted for clarity. Initially affected are the low-lying fields (*green*) originating near the polarity inversion line, in the inner band of sheared flux. Their remote ends lean increasingly far across the PIL until they come into contact with high-lying fields (*magenta*) in the outer band of sheared flux adjacent to the overlying arcade, as shown in the top left panel at time $t = 70$. When these fields reconnect, they exchange their footpoints on the far side of the PIL, as shown in the bottom left panel at time $t = 75$. As the structure continues to relax, subsequent reconnections occur that migrate the footpoint of the inner prominence field line (*green*) along the corridor of strong, sheared vertical field on the far side of the PIL. Its second reconnection partner is a more strongly sheared, high-lying field line (*magenta*) shown in the top right panel at $t = 80$. Their reconnection products, with exchanged far footpoints, are shown in the bottom right panel at $t = 85$. At the beginning of this sequence (*top left*), the inner prominence field resided completely below all of the high-lying prominence fields (*red*); at the end (*bottom right*), it loops over and closes to the surface outside of some of them. This reconfiguration puts additional stress on the high-lying fields and depresses their central portions further, as can be seen by comparing the red lines in the top left and bottom right panels.
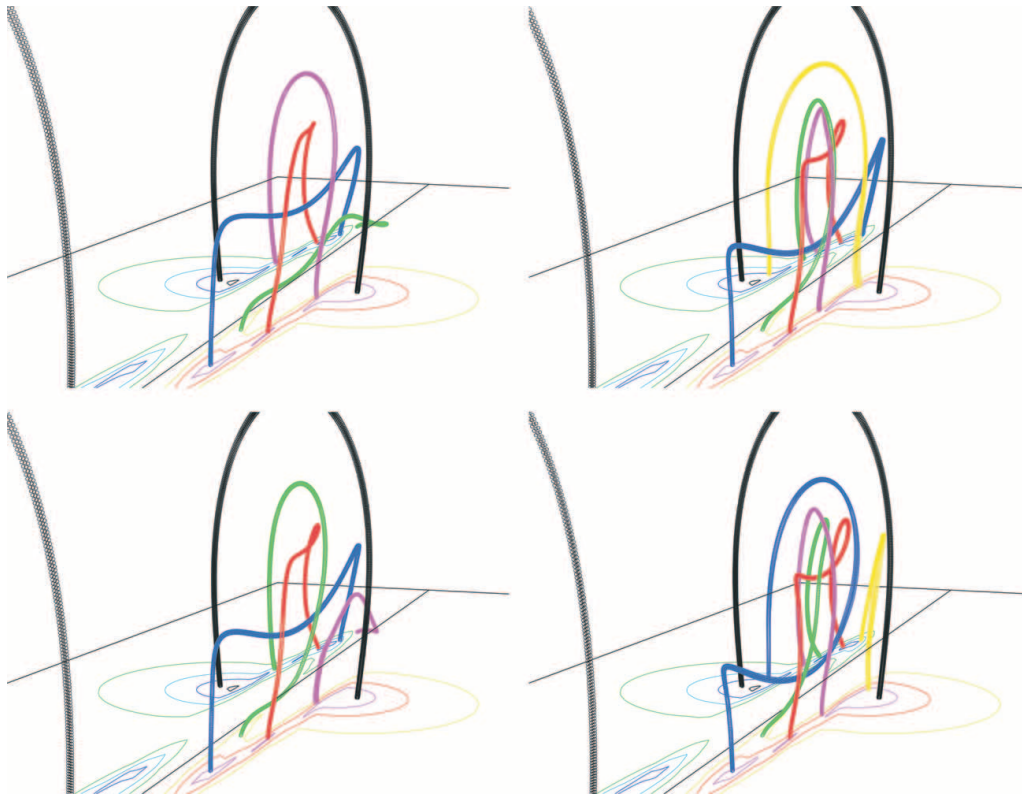
Fɪɢ. 3.—Experiment 1. Views before (*top*) and after (*bottom*) internal magnetic reconnections in the far dextral prominence, during the interaction phase (*left*, at *t* = 70 and *t* = 75; *right*, at *t* = 80 and *t* = 85) of the dextral pair whose formation was shown in Fig. 1. The pairs of reconnecting field lines are drawn in green and magenta in all four panels, and in blue and yellow in the right panels.

The right panels in Figure 3 show that the core (*blue*) prominence fields undergo reconnection with unsheared, inner-arcade fields (*yellow*) in the same manner as do the inner fields shown in the left panels. These reconnected core fields (*blue, bottom right*) loop over and close outside of both the reconnected inner fields and the unreconnected high-lying fields. This results in still more stress on the latter. However, the central portion of the core (*blue*) field remains held down by these overlying fields and retains its dipped structure. Finally, although we do not show this, later reconnections migrate the footpoints of both the inner and high-lying fields toward and eventually slightly past each other, along the corridor of strong, sheared vertical field. These events are entirely similar to those shown for the green and magenta lines in the right panels of Figure 3.

External magnetic reconnections linking the magnetic fields of the two prominences also occur in this experiment. An examination of the core fields in Figure 1 and in the left panels of Figure 3 reveals that in the region of interaction, the horizontal fields of the prominence legs are parallel. Their vertical fields, on the other hand, are antiparallel, since the legs are rooted on opposite sides of the polarity inversion line. Consequently, as the two structures close upon each other, an external current sheet forms between the advancing legs. The footpoint motion and the coronal relaxation combine to bring the prominence fields into contact at this current sheet, and magnetic reconnection ensues.

Figure 4 illustrates the reconnection process both early and late in the interaction phase, at times *t* = 70 and *t* = 75 (*left panels*) and at *t* = 120 and *t* = 125 (*right panels*). The top panels show core field lines of the two prominences (*blue and yellow*) that are converging upon each other at the external current sheet between them. The bottom panels show typical field lines that result from their reconnection: a short, arched

field line (*yellow*) links the nearby polarities of the filaments, while a long, doubly dipped field line (*blue*) connects their remote polarities. Due to this interaction, a single field line (*post-reconnection blue, bottom*) acquires essentially all of the magnetic shear that had been shared evenly between the two progenitor field lines (*pre-reconnection blue and yellow, top*). This process of shear accumulation through reconnection underlies models for both the formation of helical flux-rope prominences (van Ballegooijen & Martens 1989; van Ballegooijen 2001) and the eruption of prominences due to tether-cutting of their restraining fields (Moore & Roumeliotis 1992; Moore 2001). The newly formed, doubly sheared field lines comprise a core of magnetic flux linking our previously distinct structures. At the same time, internal field lines of our filaments that are remote from the interaction region (e.g., those shown in red and cyan) remain separate and distinct throughout the evolution.

The formation of filament-linking field lines (blue, bottom panels of Fig. 4) by reconnection opens a channel for plasma exchange between the formerly distinct prominences, carried by flows along these field lines high in the corona. Just such motions have been reported for the 1998 September 9 merger of dextral filament fragments by Deng et al. (2002). Simultaneous with these exchanges, one might anticipate the onset of upflows from either remote footpoint of the linking field lines, as well as the occurrence of downflows along their conjugate arched field lines (*yellow*). Motions of both of these types were found during the same merger event by Schmieder et al. (2004). Theoretical studies of the competition between nonuniform and/or unsteady coronal heating, thermal conduction, and optically thin radiation in the plasma along dipped magnetic field lines have been conducted by Karpen et al. (2003). They found that beyond a
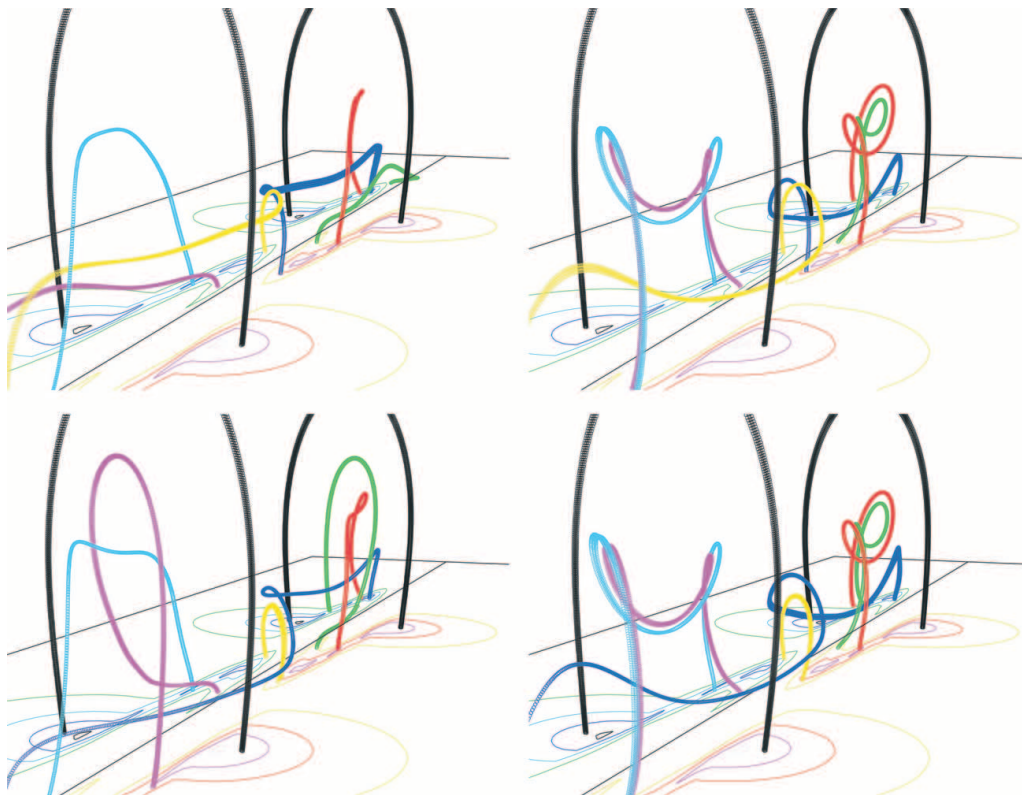
F<small>IG</small>. 4.—Experiment 1. Views before (*top*) and after (*bottom*) external magnetic reconnections between the dextral prominences shown in Figs. 1 and 3, early (*left*; at $t = 70$ and $t = 75$) and late (*right*; at $t = 120$ and $t = 125$) in the interaction phase. The blue and yellow field lines belong to the individual filaments prior to reconnecting (*top*), but link them afterward (*bottom*).

critical field-line slope (the ratio of depth to half-length of the dip) of about 10%, cool plasma condenses in the dips and remains there; below the critical slope, the condensates transit over the hump and are in a persistently dynamical state. We find that our filament-linking field lines in Figure 4 are close to the critical slope in the interaction region and below it at their far ends. Thus, their entrained plasmas should be very dynamical, with a likelihood that condensates can be exchanged across the hump in the interaction region. This behavior agrees with the observations by Deng et al. of prominence "blobs" crossing bidirectionally between their two filament fragments, as well as the upflows measured by Schmieder et al.

Deng et al. and Schmieder et al. also describe canceling photospheric flux in the interaction region between the filament fragments, which together with the observed flows is cited as evidence for magnetic reconnection. Although our experiment does not feature any flux cancellation, this is solely due to the special symmetry that we assumed. If our prominences were to converge at an oblique angle or head-on, rather than undergo the grazing collision that we imposed, we would expect to observe photospheric flux cancellation along with the other features of our present experiment. For example, both reconnection and cancellation occur in our simulation with opposite chiralities and aligned axial fields (§ 3.4).

Further inspection of the configuration shown in Figure 4 reveals that the volume below the reconnected, arched field line (*yellow, bottom panels*) is filled with similar lines whose footpoints lie successively nearer to the PIL as their apex reaches lower heights. Likewise, the volume above the reconnected, filament-linking field line (*blue, bottom panels*) contains similar linking field lines. As suggested by this sequence from early (*left panels*) to late times (*right panels*), these additional arched

and linking field lines were formed previously by the same reconnection process. A closer examination of this region shows that strongly sheared field lines reside below the developing short arcade and form a new, growing dextral prominence there (Aulanier et al. 2005). With the passage of time, the arcade of arched field lines builds, pushing upward both the interaction volume and the central portions of the new filament-linking field lines overhead. This upward expansion is restrained predominantly by the tension in the linking field lines, since the arcade fields overlying the interaction region are very weak. Consequently, an "aneurysm" forms in the magnetic flux newly linking the progenitor filaments. This structure is qualitatively similar to one whose stability has been analyzed by Sturrock et al. (2001).

One readily anticipates that applying additional footpoint displacements to the configuration in the right panels of Figure 4 would force additional reconnection between the prominence fields, raising the resulting aneurysm ever higher as the footpoints of the prominences increasingly overlap. We performed this experiment, using the same pattern and duration ($\tau = 50$) of footpoint motions as before, but only over one-half the distance ($\delta s = 3$), beginning at time $t = 150$. As shown in Figure 5, at time $t = 200$ the arched (*yellow*) and linking (*blue*) field lines have risen very high in the interaction region, as expected. Nevertheless, these linking fields remain slightly dipped to flat in the cores of the two structures, i.e., below the strong overlying (*black*) arcade fields. The unreconnected core fields of the two filaments (*red and cyan*) become highly distorted, by their approach toward and past each other and past the reconnected fields in the interaction region. Yet, their central portions also remain dipped, as can be seen in the figure.

One might expect now that the configuration in Figure 5, with its strongly distorted magnetic fields and bulging aneurysm,
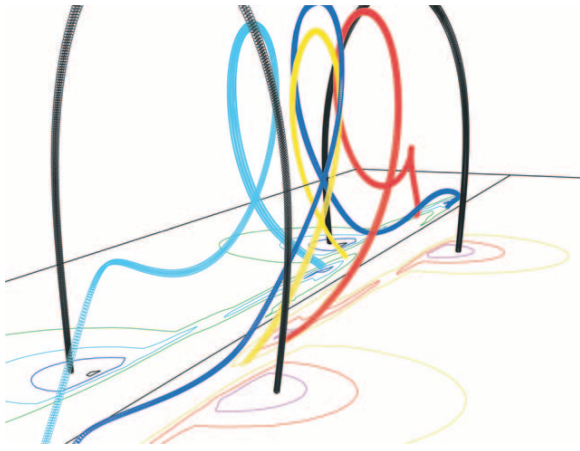
Fig. 5.—Experiment 1. A view at the end of the overlap phase ($t = 200$) of the dextral prominences shown in Figs. 1, 3, and 4. Core filament field lines (*red and cyan*) and reconnected linking field lines (*blue and yellow*), like those in the bottom panels of Fig. 4, are shown.

Fig. 6.—Evolution of the magnetic energy (*left axis, solid curve*) and kinetic energy (*right axis, dashed curve*) for the dextral prominences shown in Figs. 1, 3, 4, and 5. All energies are normalized to the energy of the initial potential field. The arrows mark break points between the formation ($t = 0–50$), interaction ($t = 50–150$), overlap ($t = 150–200$), and final relaxation ($t = 200–250$) phases.

would show signs of instability or eruption. This expectation is not borne out, however. We allowed the structure to evolve freely, with the footpoints held fixed, until time $t = 250$ was reached. No evidence for any behavior other than a simple relaxation to a new equilibrium state was found. We show the volume-integrated magnetic and kinetic energies for the full simulation, normalized to the magnetic energy of the initial potential field, in Figure 6. Qualitatively, the trends for the two footpoint-displacement episodes are identical. The magnetic energy (*solid curve*) rises slowly at first, accelerates to a peak rate of increase, then decelerates back towards a null rate of change at the conclusion, all in phase with the imposed footpoint motions. During the relaxation intervals between the displacement episodes and after the second one, the magnetic energy is approximately constant, with a very mild decline following the cessation of the imposed motions. The energies reached were about twice the initial magnetic energy, corresponding to a 100% increase, at the end of the formation phase, and about 2.25 times the initial energy, for a further 25% gain, at the end of the overlap phase.

The kinetic energy (Fig. 6, *dashed curve*) rises rapidly during both the formation and overlap phases, then declines much more slowly through the cessation of the footpoint motion and into the subsequent relaxation intervals. It peaks well after the midpoints of the intervals of imposed motion, when the footpoint velocities are greatest, due to a delay in the response of the higher coronal portions of the field. The peak kinetic energies attained were about 7% and 3.5% of the initial magnetic energy, during the formation and overlap phases, respectively. At the end of the simulation, the kinetic energy is just above 1.5% and dropping steadily. Clearly, there is no suggestion in these data of any sudden and substantial conversion of magnetic to kinetic energy, as one would expect to accompany the onset of a disruption of the configuration. The exhibited behaviors are, instead, fully consistent with an ongoing relaxation toward a new equilibrium.

3.2. *Opposite Chiralities with Opposed Axial Fields*

This experiment simulates the scenario at the bottom right in our schematic of prominence interactions, Figure 2. The initial magnetic configuration and the pattern of imposed footpoint motions are shown in the left panels of Figure 7. In order to produce a mixed prominence pair (one dextral, one sinistral), we
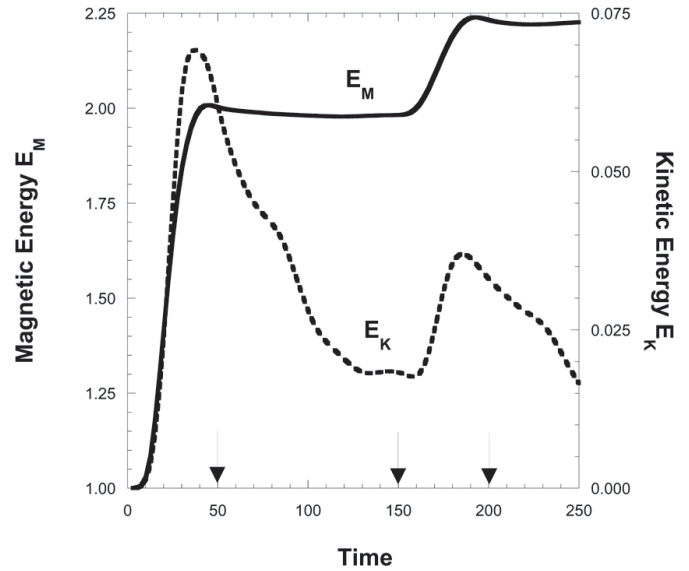
reversed the direction of the imposed footpoint motions in the half-plane $x < 0$ (i.e., to the left or in the foreground in each panel) relative to our first case. This causes the advancing photospheric fluxes of the developing prominences to collide head-on on one side of the polarity inversion line, rather than to undergo a glancing collision from opposite sides of the PIL as before. Therefore, we placed the initial point bipoles slightly farther apart, at $x = s = \pm 7$, compared to ± 6 previously. These changes can be seen by comparing the left panels of Figures 1 and 7. At time $t = 40$, near the end of the formation phase, the field has attained the configuration shown in the right panels of Figure 7. The dextral prominence, at the right or in the background, is essentially identical to its correspondent in Figure 1; the sinistral prominence, at the left or in the foreground, is the mirror image of its dextral companion. Thus, this configuration contains zero net magnetic helicity. This experiment models the formation of and interaction between dextral and sinistral filaments along a shared PIL in a bipolar magnetic topology, such as the events described by Martin et al. (1994) and Schmieder et al. (2004).

As can be seen in Figure 7, in the interaction region the vertical and transverse horizontal fields in the legs of the two prominences are parallel; only their axial fields are antiparallel. In contrast to the previous case, then, no current sheet forms between the advancing legs and no linking reconnections take place. The field strength and magnetic pressure build inexorably in the interaction region as the two structures close upon each other. After the footpoint motions are arrested, the individual filaments become increasingly distorted from their preinteraction shapes as the configuration relaxes toward equilibrium. Since no external reconnections occur between them, however, no linking field lines form, and the filaments retain their separate identities.

In a more general situation without the high symmetry of this idealized experiment, we can envision readily that the fields of the two filaments in the plane of interaction would not be perfectly parallel. For example, the filament ends might approach
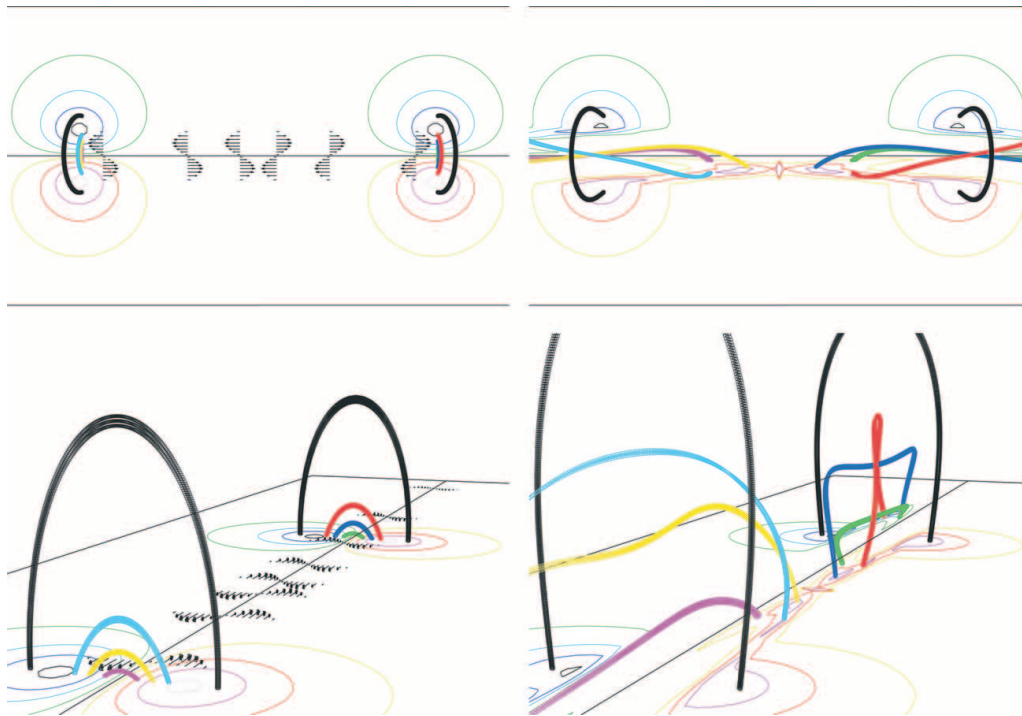
Fig. 7.—Experiment 2. Overhead (*top*) and perspective (*bottom*) views of a dextral prominence (*right or background in each panel*) interacting with a sinistral prominence (*left or foreground in each panel*), for both the initial state ($t = 0$; *left*) and the configuration near the end of the formation phase and the beginning of the interaction phase ($t = 40$; *right*). The axial field of the dextral prominence points from left to right or foreground to background, as in Fig. 1, but that of the sinistral prominence points in the opposite direction. This simulation is described in § 3.2.

each other at an oblique angle, rather than precisely head-on as assumed here. External current sheets then could form between the advancing legs, leading to reconnections between their fields. Even were that to occur, however, no linking field lines would be produced: the far vertical polarities of the two prominences are identical and cannot be connected directly by a coronal field line. These external reconnections in a less symmetric encounter would produce only exchanges of footpoints of the field lines between the advancing fluxes of the two filaments, thereby commingling their feet. We show examples of this in the experiment with identical chiralities and opposed axial fields (§ 3.3).

Our resultant configuration at time $t = 75$ is shown in Figure 8. Although the field continues to relax at this stage, we stopped the simulation here. Progress is very slow due to the high field strength and small grid spacing in the interaction region, which together severely reduce the numerical time step. The magnetic and kinetic energies differ only slightly from those shown in Figure 6 for our first experiment. At the end, the magnetic energy curve is flat at twice the initial value and the kinetic energy is dropping steadily through 4%, as the system apparently relaxes toward equilibrium. We expect that the subsequent evolution of the energies would follow qualitatively that described previously, and also that the sequence of internal reconnections within the individual prominences would proceed as before. The latter is supported by our findings for the case of opposite chiralities with aligned axial fields (§ 3.4).

Comparing the overhead views of the filaments in the top right panel of Figure 7 and the top panel of Figure 8, we find that the core blue and yellow field lines lean progressively farther over the photospheric PIL as their footpoints approach the interaction region. They also rise higher at their neighboring ends than at their remote ends, as can be seen in the bottom panel of Figure 8, due to the magnetic pressure enhancement. In
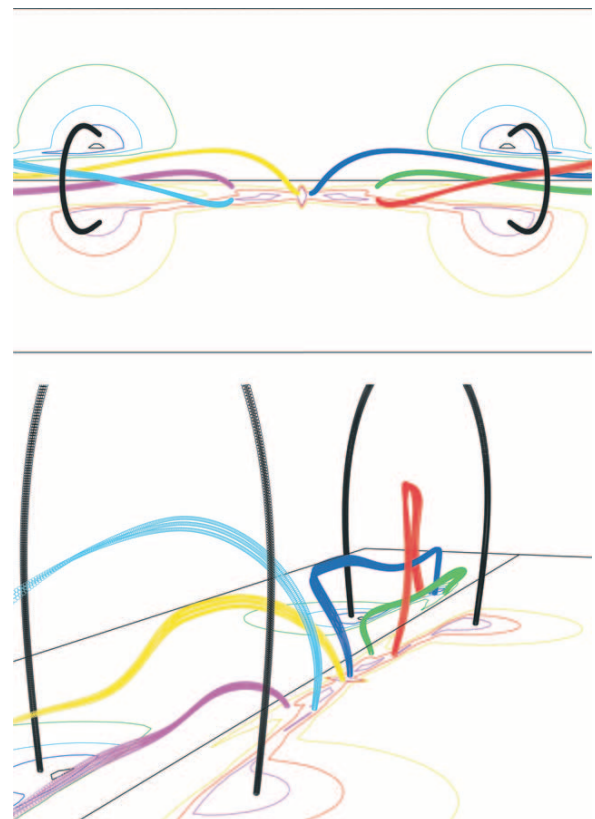

Fig. 8.—Experiment 2. Overhead (*top*) and perspective (*bottom*) views during the interaction phase ($t = 75$) of the dextral and sinistral prominences whose formation was shown in Fig. 7.

appearance, this evolution should exhibit a cusp developing in the interaction region: the flattened and dipped portions of the field lines that host the prominence plasma increasingly flare across the PIL (due to the leaning) and also retreat from the interaction region (due to the rising) as the two structures converge upon each other. This behavior is consistent with the observations reported by Martin et al. and Schmieder et al.

3.3. *Identical Chiralities with Opposed Axial Fields*

Our objective in this experiment is to form a pair of prominences with identical chiralities, as in our first experiment, but with opposed axial fields. The axial fields of those prominences were aligned because the point dipoles constituting their initial arcade fields were parallel. Thus, we could repeat that simulation after reversing the direction of one of the dipoles, say at the left or in the foreground of Figure 1. The photospheric radial field then would assume a quadrupolar distribution, as indicated schematically in the top right panel of Figure 2, with a second polarity inversion line crossing the one shared by the two prominences. However, the initial potential field so computed also would contain, from the outset, magnetic connections between the weaker fields of the two arcades across this second PIL. To avoid this, we chose instead to take the initial field in Figure 1 and simply reverse the sign of all fields in the half-space $x < 0$. On our staggered mesh, only the x magnetic field components B_x are defined precisely at $x = 0$, on the x faces of the grid cells (DeVore 1991). By symmetry, however, B_x vanishes there in our first experiment. Thus, reversing the fields for $x < 0$ magnetically isolates the two arcade-plus-prominence systems from each other, while simultaneously keeping the field divergence-free everywhere.

From the outset of this simulation, a current sheet occupies the plane $x = 0$ since the transverse components of the field reverse direction across it. One might anticipate, and indeed we observe, that the imposed footpoint motions drive reconnections between the weak arcade fields across this current sheet. This process converts pairs of overlying arcade field lines closing across the first PIL into pairs of arches that close across the second PIL, whose tops then recede from the interaction region toward the sides. However, these reconfigurations have no discernible effect on the evolution of the strong core fields of our structures.

Applying the same footpoint displacements shown in Figure 1 again forms a pair of dextral prominences. The early evolution is very similar to that obtained in our first experiment, except for the anticipated reconnections between weak arcade fields. Indeed, swapping the colors of the vertical-field contours across the shared PIL at the left or in the foreground in Figure 1 yields a visualization of the strong filament and arcade fields for the present case. The mirror image of that resulting figure—which we also could obtain by reversing the direction of the imposed footpoint motions in the simulation—models the corresponding case of a pair of sinistral filaments forming and coming into contact with each other with their axial fields opposed.

In this experiment, conversely to our first, the horizontal fields in the legs of the prominences are antiparallel, while their vertical fields are parallel. Therefore, an external current sheet again forms between the converging structures, and magnetic reconnection eventually ensues. This reconnection process is illustrated in Figure 9, early in the interaction phase at times $t = 70$ and $t = 75$. Core field lines of the two prominences (*blue and yellow*) converging upon each other at the current sheet between the legs are shown in the top panel. The field lines that result from their reconnection are shown in the bottom panel.
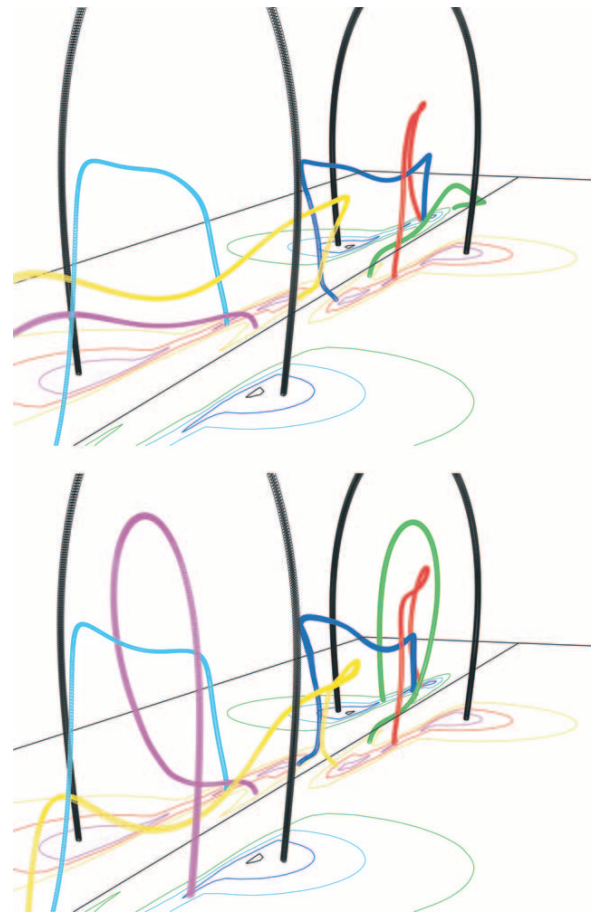

Fig. 9.—Experiment 3. Views before (*top*) and after (*bottom*) external magnetic reconnections between dextral prominences, early in the interaction phase at times $t = 70$ and $t = 75$. The blue and yellow field lines belong to the individual filaments both before and after reconnecting, but exchange their footpoints across the polarity inversion line. The axial field of the far prominence points from foreground to background, as before, while that of the near prominence points in the opposite direction. This simulation is described in § 3.3.

They link the trailing photospheric flux of each prominence with the advancing flux of the other; i.e., the pre-reconnection field lines exchange footpoints across the intersecting polarity inversion lines separating their photospheric fluxes. This has the effect of commingling the advancing legs and feet of the two prominences, effectively spreading the feet and broadening the ends of the prominences as their reconnected fields relax across the shared PIL. At the same time, the amount of shear on each individual field line is approximately preserved during this footpoint exchange. As in our previous experiment, linking field lines that join the structures end-to-end cannot form: the axial fields of the two filaments are opposed, or equivalently, the vertical fields at their remote ends have the same polarity.

Snapshots of the subsequent evolution of the footpoint-exchanging field lines of Figure 9 are shown in Figure 10. The blue field line is always drawn from the advancing flux of the far prominence, the yellow from that of the near prominence. The remote footpoints of these field lines switch back and forth between the trailing flux of either prominence; i.e., these lines undergo both the forward reconnection process shown in Figure 9 and its reverse. Their footpoints also can switch to the inner arcade flux of either prominence—e.g., the yellow line in the bottom left panel and the blue line in the top right—due to internal reconnections between the strongly and weakly sheared
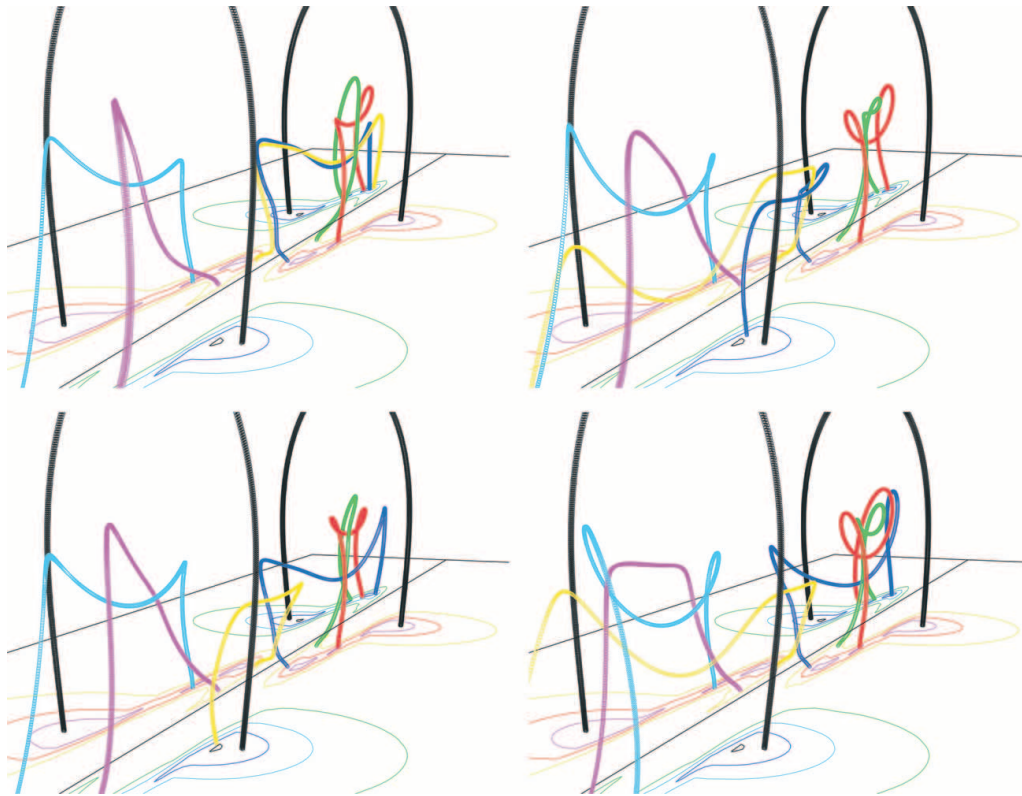
FIG. 10.—Experiment 3. Views showing subsequent external magnetic reconnections between the dextral prominences shown in Fig. 9, at times $t = 85$ (*top left*), $t = 95$ (*bottom left*), $t = 105$ (*top right*), and $t = 115$ (*bottom right*) in the interaction phase. The starting footpoints of the blue and yellow field lines in the advancing fluxes of the two prominences are held fixed throughout, at the same positions as in Fig. 9.

fields within either structure. These multiple bidirectional reconnections have restored, at the latest time ($t = 115$) shown in Figure 10, the connectivity of the field lines that prevailed at the earliest time ($t = 70$) shown in Figure 9. This behavior contrasts with the unidirectional reconnections evident in our first experiment, wherein the reconnected linking field lines relaxed upward and out of the interaction region, so that the reverse reconnection process did not occur. Here the reconnected field lines cannot withdraw from the interaction region as they relax, and so they are vulnerable to subsequent reconnection events that switch their footpoints back and forth between the prominences. This dynamical footpoint switching evidently will persist until all disturbances on the participating field lines are dissipated away.

3.4. *Opposite Chiralities with Aligned Axial Fields*

The preparation of our fourth and final experiment begins with the initial magnetic field for the case of opposite chiralities and opposed axial fields, described in § 3.2 and shown in Figure 7. As discussed in the preceding subsection, we reverse the sign of all magnetic fields in the half-space $x < 0$, producing a quadrupolar distribution of vertical flux at the photosphere and a weak current sheet in the $x = 0$ plane. Imposing the same footpoint motions shown in Figure 7 again forms a dextral filament at the right (or in the background) of each panel and a sinistral filament at the left (or in the foreground). This time, however, the axial fields of the filaments point in the same direction, as in the schematic at the bottom left in Figure 2.

The configuration of the field lines early in this experiment differs little from that illustrated in Figure 7. Of course, the sign of the vertical field is reversed at the left or in the foreground of those images. As the evolution proceeds, the weak arcade fields reconnect across the current sheet separating them, but again with

no discernible effect on the strong filament and arcade fields. In our prior experiment, we found that the filaments were increasingly distorted by the close approach of their converging ends, shown in Figure 8. This occurs in the present experiment as well. Here, however, the vertical fields in the converging filament legs are antiparallel and so cancel each other at the photosphere, instead of accumulating as they do when parallel. Consequently, the field strength and the numerical time step remained moderate throughout this simulation, which we continued much farther into the interaction phase than its predecessor.

The vertical and transverse horizontal fields of the prominence legs are antiparallel in the interaction region; only the locally weak, axial fields are aligned. Thus, an external current sheet again develops between the converging filaments, promoting external reconnections between the fields of the two structures. This process is shown early (at $t = 70$ and $t = 75$) in the interaction phase, in the left panels of Figure 11. Pre-reconnection core fields of the prominences (*blue and yellow*) are shown at the top left. The products of the reconnection are new short loops (*yellow*) connecting the nearby fluxes of the formerly separate filaments, and long field lines with multiple dips (*blue*) linking the remote fluxes to each other, shown at the bottom left. These linking field lines subsequently adjust as internal reconnections within each prominence dominate the dynamics later in the interaction phase, as shown in the right panels (at $t = 100$ and $t = 125$) of Figure 11.

Topologically, the results of this numerical experiment are essentially identical to those of our first, in § 3.1: newly formed field lines acquire essentially twice the shear of the progenitor fields of the individual prominences and link the two structures end to end. The linking fields coexist with other fields, internal to the initially separate prominences, that remain disconnected from
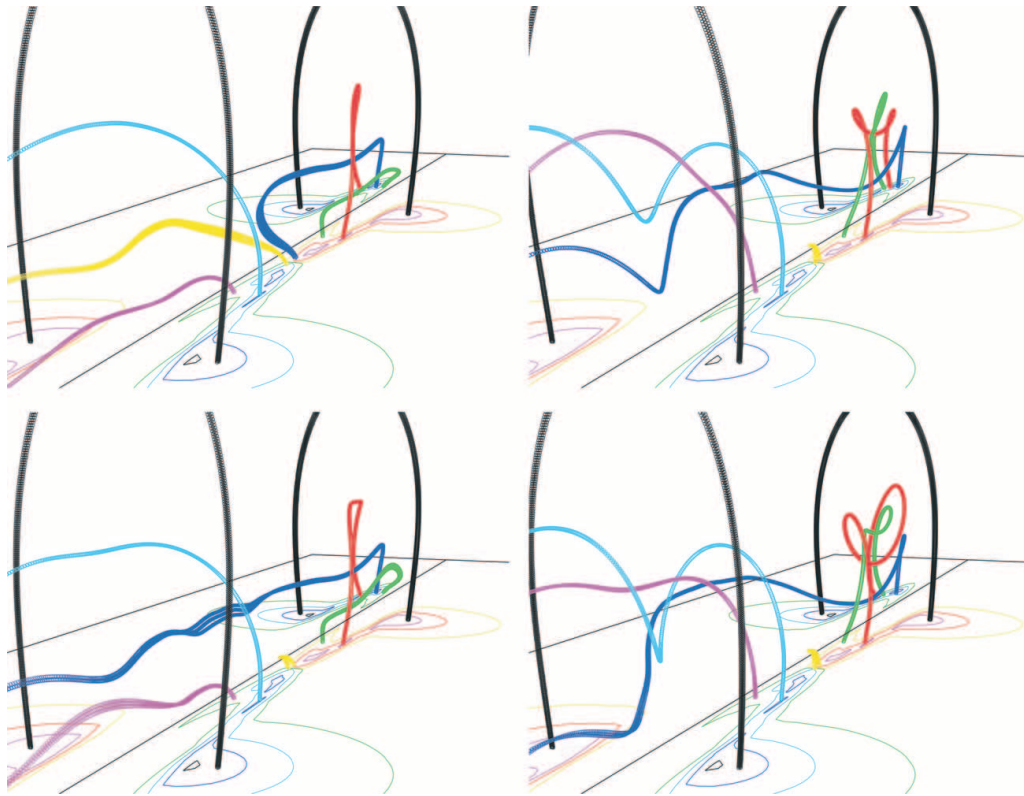
Fig. 11.—Experiment 4. Views before (*top left*) and after external magnetic reconnections between dextral and sinistral prominences, early (*left*; at $t = 70$ and $t = 75$) and late (*right*; at $t = 100$ and $t = 125$) in the interaction phase. Blue and yellow field lines belong to the individual filaments prior to reconnecting, but link them afterward. The axial field points from foreground to background in both prominences. This simulation is described in § 3.4.

each other throughout the evolution. Multiple internal reconnections reconfigure each prominence as the interaction proceeds. Quantitatively, the magnetic and kinetic energies differ only very slightly from those obtained before, and their temporal trends are qualitatively identical. Again, we find evidence only for a gradual relaxation to an apparently stable new equilibrium state.

4. DISCUSSION

We have conducted numerical experiments that test the four possible fundamental combinations of interactions between pairs of solar prominences: identical or opposite chiralities, and aligned or opposed axial magnetic fields. From the viewpoint of magnetic reconnection theory, we would expect that prominences with aligned axial magnetic fields should be susceptible to linkage-producing interactions, irrespective of their chiralities. The alignment of the axial fields implies that the vertical fields in the converging prominence legs are antiparallel, so that a current sheet forms and strengthens between them as they approach. Eventually, reconnection will ensue and form field lines that connect the formerly distinct structures. This is the essential result of our experiments in § 3.1 (identical chiralities) and § 3.4 (opposite chiralities).

Conversely, theory suggests that prominences with opposed axial fields cannot be linked together, whatever their chiralities. The opposition of the axial fields implies that the vertical fields in the far legs have the same polarity, prohibiting connections between them and leaving the structures separate and distinct. This is the conclusion of our experiments in § 3.2 (opposite chiralities) and § 3.3 (identical chiralities). In the latter experiment, some reconnections occur between the prominence legs because their transverse horizontal fields are antiparallel; in the former, such reconnections are not observed because

the transverse horizontal fields are parallel. These interactions do not produce field lines that link the two prominences, however. Rather, their effect is to exchange footpoints of field lines between the converging prominence feet. We anticipate observing such reconnections also in the case of opposite chiralities, if the high symmetry of our experiment in § 3.2 were broken, e.g., due to a sufficiently oblique trajectory of the converging legs.

There is an apparent contradiction between the predictions of reconnection theory and the results of our numerical experiments, on the one hand, and the empirical rules of prominence interactions on the other. The latter state that prominences with identical chiralities will link up to form conjoined structures, while those with opposite chiralities will avoid each other and remain disconnected (Martin et al. 1994; Rust 2001; Schmieder et al. 2004). For the simplest and most common situations in which the topology of the combined flux systems is bipolar, i.e., a single polarity inversion line is shared by the two prominences, these disparate findings are reconciled. In this case, there is a one-to-one correspondence between filament chirality and axial field alignment: identical chiralities imply aligned axial fields and linkage (§ 3.1), whereas opposite chiralities imply opposed axial fields and avoidance (§ 3.2). Thus, theory, simulation, and observation all agree for prominence interactions in bipolar topologies.

The situations in which theory and simulation conflict with the stated empirical rules exhibit a quadrupolar topology of the combined flux systems, in which the polarity inversion line shared by the prominences is crossed by a secondary PIL. Once again, there is a one-to-one correspondence between filament chirality and axial field alignment, but it is the converse of that for bipolar topologies: identical chiralities imply opposed axial

fields (§ 3.3), whereas opposite chiralities imply aligned axial fields (§ 3.4). In this case, the resultant prominence interactions are the converse of the usual empirical rule: prominences with opposite chiralities can link up to form conjoined structures (§ 3.4), while those with identical chiralities can only commingle their neighboring feet by exchanging field-line footpoints between them (§ 3.3).

We are unaware of any documented observations of prominence interactions in these more complex, quadrupolar configurations. Indeed, we have found only two cited examples (Martin et al. 1994; Rust 2001; Schmieder et al. 2004) of the avoidance of opposite-chirality prominences, which occurred in bipolar topologies. It seems plausible that our "converse rule" for quadrupolar topologies is simply untested by any observations analyzed to date. We encourage tests of this rule in future observations of prominence interactions, if suitable candidate events can be found.

Lengthy sequences of high-resolution images in the wings of Hα have shown steady bidirectional motions of knots of emission within filaments, particularly along their spines, which evidently reveal counterstreaming flows of plasma along magnetic field lines (Zirker et al. 1998; Deng et al. 2002). At 10 km s^{-1}, these knots can traverse 10^5 km along a field line in about 3 hr. A similar sequence of images of a pair of interacting filaments, especially in a geometry favorably disposed to reconnection and linkage, could be extremely interesting to analyze and interpret. We would expect to observe a transition from solely disjoint motions in the two preinteraction entities to a mixture that includes correlated motions traversing a sizable fraction of the newly linked structure (Deng et al. observed the linked motions, but not the transition beforehand). Such a result would constitute perhaps the most compelling direct evidence yet for magnetic reconnection in the corona, in general, as well as provide considerable insight into the dynamics of prominence interactions in particular.

Some observations suggest that the process of linkage by magnetic reconnection can initiate a disruption of the combined structure. Pevtsov et al. (1996) describe the linkage of a pair of twisted X-ray loops, followed promptly by a two-ribbon flare and the eruption of an Hα filament underlying one of the loops. They conclude that the twist on the linked field lines exceeded the threshold for an ideal kink instability, thereby initiating the ejection. Uralov et al. (2002) observed a pair of interacting dextral filaments that subsequently erupted as a single structure. They ascribe their event to a loss of equilibrium driven by a combination of flux cancellation between opposite-polarity barbs, formation of helical field lines, and tether-cutting reconnection (Moore & Roumeliotis 1992; Moore 2001) of the restraining arcade fields below the rising filament. Other filament linkage events, accompanied by formation of an aneurysm in the inter-action region and followed by the eruption of the linked structure, have been described to us from *Transition Region and Coronal Explorer* (*TRACE*) EUV data (A. M. Title 2000 and L. Fletcher 2001, private communications) but have not yet been reported in print. At the same time, however, it is clear that the merger of filament fragments instead can produce quite innocuous activations, evidenced by enhanced plasma emissions, oscillations, and transient flows but no disruption (Martin et al. 1994; Deng et al. 2002; van Ballegooijen 2004; Schmieder et al. 2004).

Our numerical experiments clearly show evidence for prominence linkage through tether-cutting reconnection (§§ 3.1 and 3.4), the formation of helical field lines and an aneurysm (§ 3.1), and flux cancellation between encroaching prominence feet (§ 3.4). Nevertheless, we find no indication of the onset of instability, loss of equilibrium, or initiation of an eruption in any of our experiments. Although a rather strong magnetic shear is introduced, it is possible that our magnetic field contains an insufficient amount of twist even on the reconnected, linking field lines. A field line displaced far along the polarity inversion line contains an effective twist of $\pi/2$ at each footpoint, or π overall, corresponding to one half-turn along an individual prominence. Our linking field lines therefore contain twice that, i.e., 2π of twist or one full-turn. This is less than the 2.5π of twist found sufficient by Pevtsov et al. for kink instability of their reconnected X-ray loop, and less than the 2.4π of twist deemed necessary by Sturrock et al. (2001) to split the arcade overlying a force-free flux rope and eject the bulging portion of the rope to infinity. Our results cannot rule out the latter scenario, but they do support a plausible alternative: the arcade will split quietly and allow the aneurysm to bulge outward gradually, as the energy in the twisted flux rope and arcade rises toward that of the open configuration. Time-dependent numerical experiments are required to determine which of these outcomes is favored in nature. Such simulations could be conducted within the framework of our study, either by appropriately twisting the arcade fields before applying the linear footpoint displacements or by linking together three or more of our filaments.

REFERENCES

Antiochos, S. K., Dahlburg, R. B., & Klimchuk, J. A. 1994, ApJ, 420, L41
Aulanier, G., DeVore, C. R., & Antiochos, S. K. 2002, ApJ, 567, L97
———. 2005, ApJ, submitted
Babcock, H. W. 1953, ApJ, 118, 387
Babcock, H. W., & Babcock, H. D. 1955, ApJ, 121, 349
Berger, M. A. 1998, in IAU Colloq. 167, New Perspectives on Solar Prominences, ed. D. Webb, D. Rust, & B. Schmieder (ASP Conf. Ser. 150; San Francisco: ASP), 102
Chae, J., Wang, H., Qiu, J., Goode, P. R., Strous, L., & Yun, H. S. 2001, ApJ, 560, 476
d'Azambuja, L., & d'Azambuja, M. 1948, Ann. Obs. Paris Meudon, 6, 7
Deng, Y., Lin, Y., Schmieder, B., & Engvold, O. 2002, Sol. Phys., 209, 153
DeVore, C. R. 1991, J. Comput. Phys., 92, 142

DeVore, C. R., & Antiochos, S. K. 2000, ApJ, 539, 954
Foukal, P. 1971, Sol. Phys., 19, 59
Gaizauskas, V. 2001, in Encyclopedia of Astronomy and Astrophysics, ed. P. Murdin (Philadelphia: Nature), http://eaa.iop.org
Glover, A., Harra, L. K., Matthews, S. A., Hori, K., & Culhane, J. L. 2001, A&A, 378, 239
Karpen, J. T., Antiochos, S. K., Klimchuk, J. A., & MacNeice, P. J. 2003, ApJ, 593, 1187
Martin, S. F. 1998, Sol. Phys., 182, 107
———. 2001, in Encyclopedia of Astronomy and Astrophysics, ed. P. Murdin (Philadelphia: Nature), http://eaa.iop.org
Martin, S. F., Bilimoria, R., & Tracadas, P. W. 1994, in Solar Surface Magnetism, ed. R. J. Rutten & C. J. Schrijver (NATO ASI Ser. C, 433; Dordrecht: Kluwer), 303

Martin, S. F., & McAllister, A. H. 1996, in IAU Colloq. 153, Magnetodynamic Phenomena in the Solar Atmosphere, ed. Y. Uchida, H. S. Hudson, & T. Kosugi (Dordrecht: Kluwer), 497

Moon, Y.-J., Chae, J., Choe, G. S., Wang, H., Park, Y. D., Yun, H. S., Yurchyshyn, V., & Goode, P. R. 2002, ApJ, 574, 1066

Moore, R. M. 2001, in Encyclopedia of Astronomy and Astrophysics, ed. P. Murdin (Philadelphia: Nature), http://eaa.iop.org

Moore, R. M., & Roumeliotis, G. 1992, in IAU Colloq. 133, Eruptive Solar Flares, ed. Z. Svestka, B. V. Jackson, & M. E. Machado (New York: Springer), 69

Pevtsov, A. A., Canfield, R. C., & Zirin, H. 1996, ApJ, 473, 533

Pevtsov, A. A., Maleev, V. M., & Longcope, D. W. 2003, ApJ, 593, 1217

Priest, E. R., ed. 1989, Dynamics and Structure of Quiescent Solar Prominences (Dordrecht: Kluwer)

Rust, D. M. 1967, ApJ, 150, 313

———. 2001, in Encyclopedia of Astronomy and Astrophysics, ed. P. Murdin (Philadelphia: Nature), http://eaa.iop.org

Ruzdjak, V., & Tandberg-Hanssen, E., eds. 1990, IAU Colloq. 117, Dynamics of Quiescent Prominences (New York: Springer)

Schmieder, B., Mein, N., Deng, Y., Dumitrache, C., Malherbe, J.-M., Staiger, J., & DeLuca, E. E. 2004, Sol. Phys., 223, 119

Sturrock, P. A., Weber, M., Wheatland, M. S., & Wolfson, R. 2001, ApJ, 548, 492

Tandberg-Hanssen, E. 1974, Solar Prominences (Dordrecht: Reidel)

———. 1995, The Nature of Solar Prominences (Dordrecht: Kluwer)

Uralov, A. M., Lesovoi, S. V., Zandanov, V. G., & Grechnev, V. V. 2002, Sol. Phys., 208, 69

van Ballegooijen, A. A. 2001, in Encyclopedia of Astronomy and Astrophysics, ed. P. Murdin (Philadelphia: Nature), http://eaa.iop.org

———. 2004, ApJ, 612, 519

van Ballegooijen, A. A., & Martens, P. C. H. 1989, ApJ, 343, 971

Webb, D., Rust, D., & Schmieder, B., eds. 1998, IAU Colloq. 167, New Perspectives on Solar Prominences (ASP Conf. Ser. 150; San Francisco: ASP)

Zirin, H., & Severny, A. B. 1961, Observatory, 81, 155

Zirker, J. B. 2001, in Encyclopedia of Astronomy and Astrophysics, ed. P. Murdin (Philadelphia: Nature), http://eaa.iop.org

Zirker, J. B., Engvold, O., & Martin, S. F. 1998, Nature, 396, 440